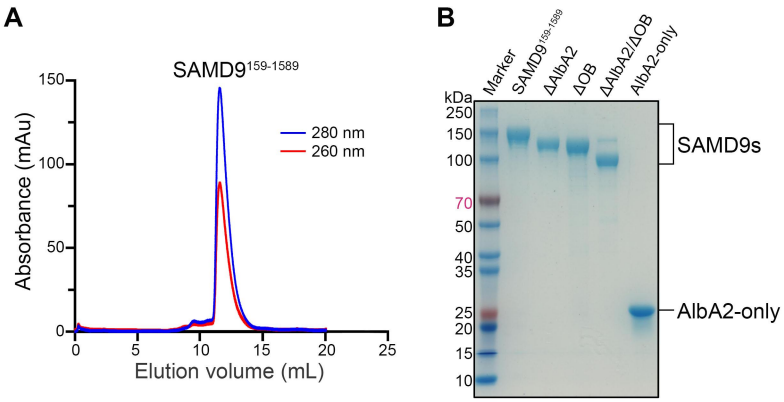

Supplementary Figure S1. Expression and purification of human SAMD9C and its domain-truncation variants

(**A**) Representative size-exclusion chromatography (SEC) profile of purified wild-type human SAMD9C (residues 159–1589) on a Superdex 200 Increase 10/300 GL column, showing a monodisperse peak. Absorbances at 280 nm (protein, blue trace) and 260 nm (red trace) are monitored.

(**B**) SDS-PAGE analysis of purified SAMD9C and its domain-truncation variants (ΔAlbA2, ΔOB, ΔAlbA2/ΔOB, and the AlbA2-only construct), confirming protein purity and apparent molecular weights. Molecular weight markers (kDa) are indicated on the left.

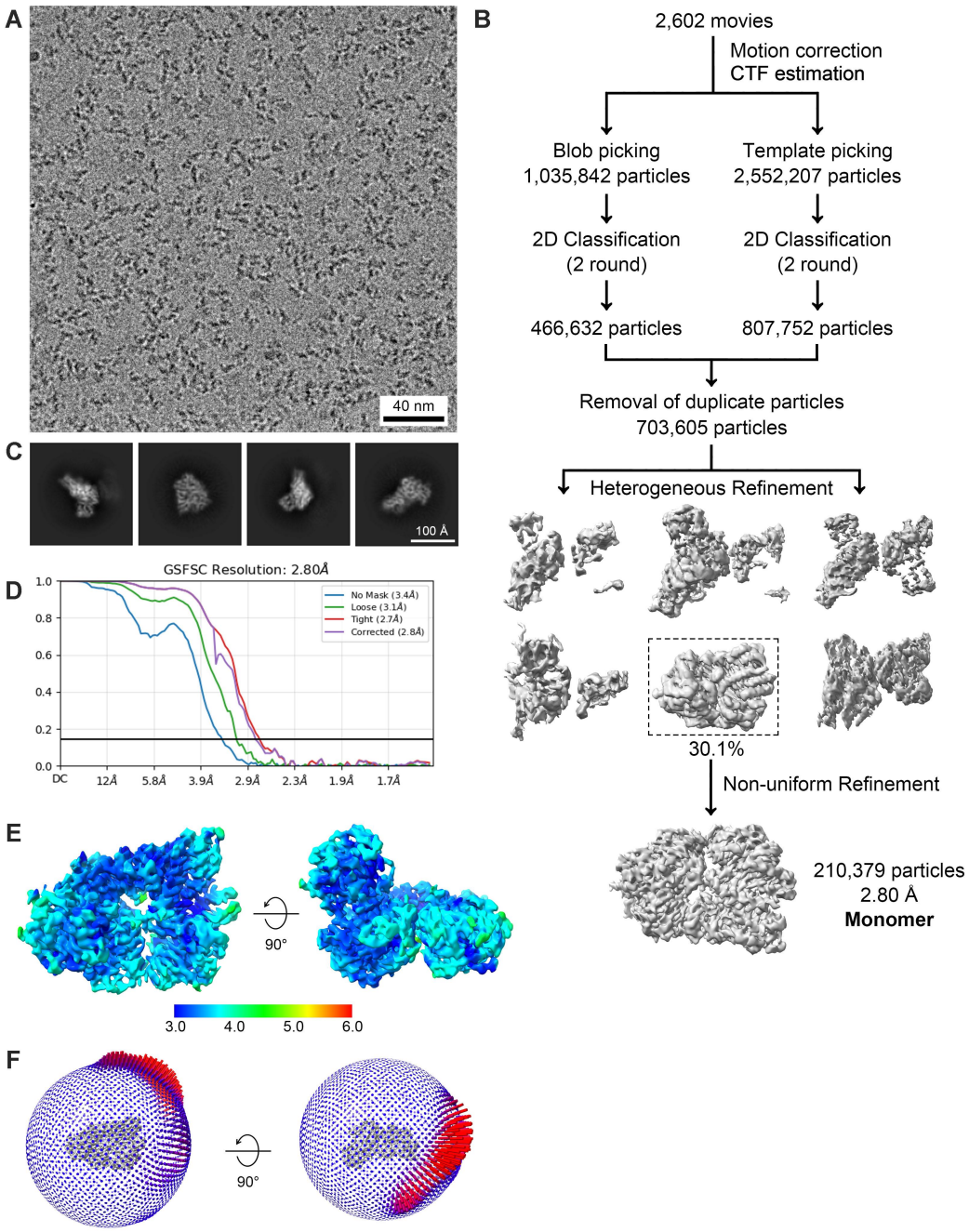

Supplementary Figure S2. Cryo-EM data processing and single-particle reconstruction of SAMD9C
(**A**) Representative cryo-EM micrograph of SAMD9C. Scale bar, 40 nm.
(**B**) Flowchart of cryo-EM data processing workflow. From 2,602 movies, initial particle picking yielded 1,035,842 particles via blob picking and 2,552,207 particles via template picking. After two rounds of 2D classification and removal of duplicate particles, a cleaned dataset of 703,605 particles was selected. Subsequent heterogeneous refinement and non-uniform refinement generated a final 2.80 Å map of the compact SAMD9C monomer from 210,379 particles.
(**C**) Representative 2D class averages of the SAMD9C monomer, displaying clear structural features and diverse orientations. Scale bar, 100 Å.
(**D**) Gold-standard Fourier shell correlation (FSC) curves for the final reconstruction, indicating a global resolution of 2.80 Å based on the FSC = 0.143 criterion.
(**E**) Two orthogonal views of the local resolution map for the SAMD9C monomer estimated in cryoSPARC; the resolution color scale (Å) is displayed below.
(**F**) Angular distribution heatmap of particles included in the final 3D reconstruction.

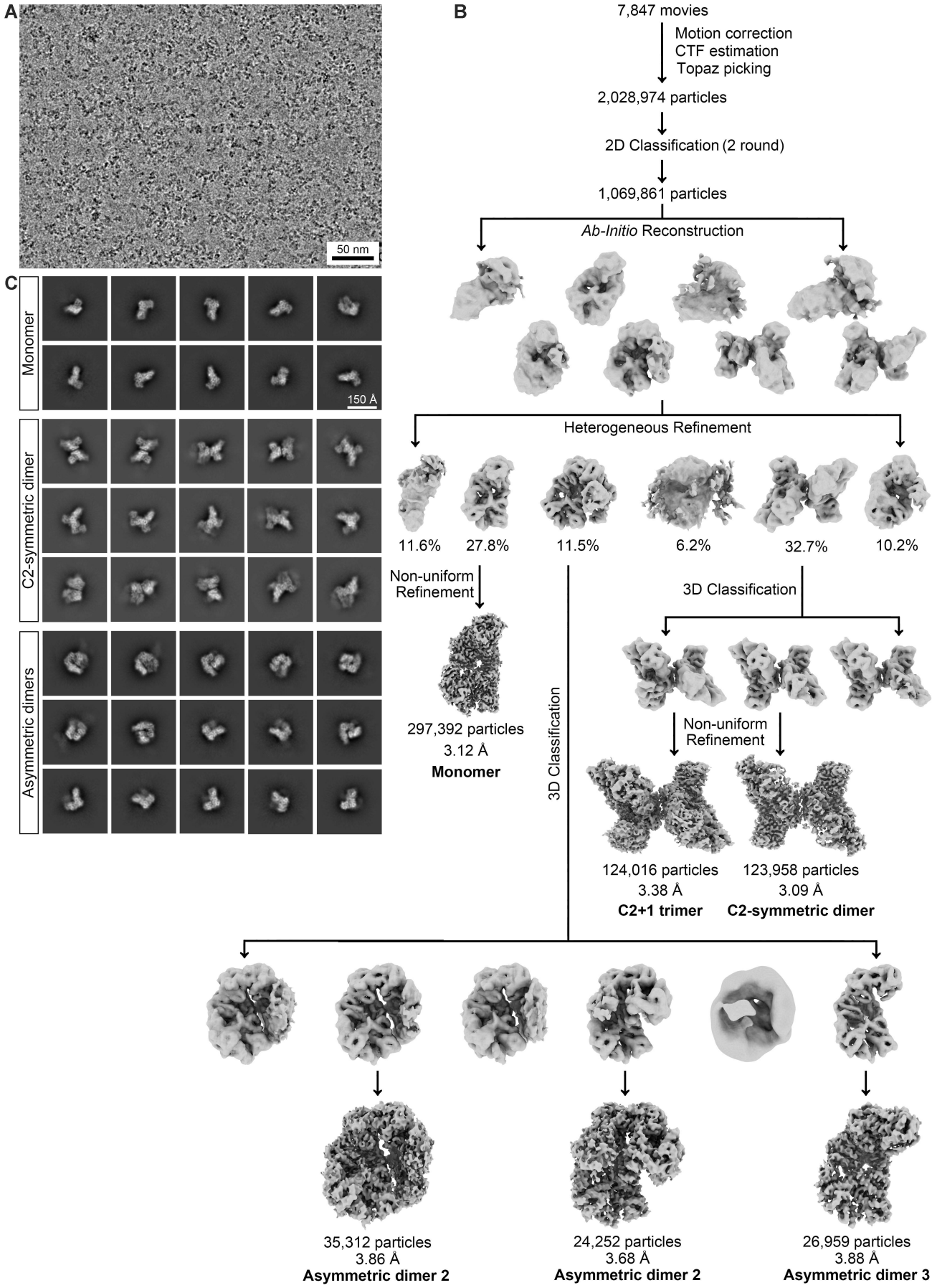
A
50 nm
B
7,847 movies
Motion correction
CTF estimation
Topaz picking
2,028,974 particles
2D Classification (2 round)
1,069,861 particles
Ab-Initio Reconstruction
Heterogeneous Refinement
11.6%
27.8%
11.5%
6.2%
32.7%
10.2%
Non-uniform Refinement
297,392 particles
3.12 Å
Monomer
3D Classification
3D Classification
Non-uniform Refinement
124,016 particles
3.38 Å
C2+1 trimer
123,958 particles
3.09 Å
C2-symmetric dimer
35,312 particles
3.86 Å
Asymmetric dimer 2
24,252 particles
3.68 Å
Asymmetric dimer 2
26,959 particles
3.88 Å
Asymmetric dimer 3
C
Monomer
C2-symmetric dimer
Asymmetric dimers
150 Å

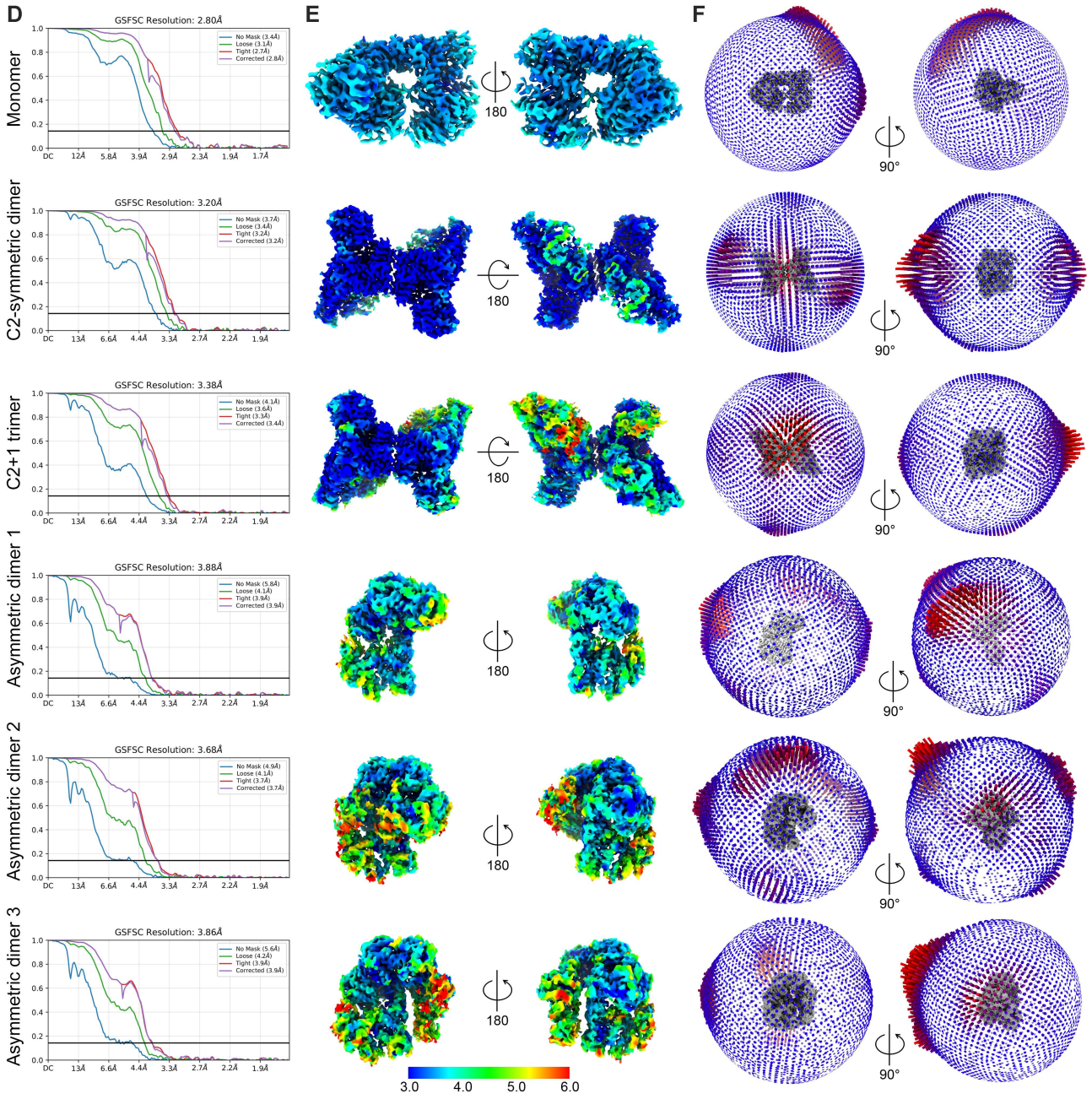

Supplementary Figure S3. Cryo-EM data processing and single-particle reconstruction of SAMD9C in distinct conformational states

(**A**) Representative cryo-EM micrograph. Scale bar, 50 nm.

(**B**) Flowchart of cryo-EM data processing workflow. From 7,847 movies, initial particle picking yielded 2,028,974 particles via Topaz picking. Following two rounds of 2D classification, a cleaned dataset of 1,069,861 particles was subjected to *ab initio* reconstruction and heterogeneous refinement. Subsequent 3D classification and non-uniform refinement yielded six distinct conformational maps: monomer (3.12 Å, 297,392 particles), two C_2-symmetric dimers (3.20 Å, 123,958 particles; 3.01 Å, 225,953 particles;), C_2+1 trimer (3.38 Å, 124,016 particles), asymmetric dimer 1 (3.86 Å, 35,312 particles), asymmetric dimer 2 (3.68 Å, 24,252 particles), and asymmetric dimer 3 (3.88 Å, 26,959 particles).

(**C**) Representative 2D class averages showing distinct structural features for the monomer (top), C_2-symmetric dimer and C_2+1 trimer (middle), and asymmetric dimers (bottom). Scale bar, 150 Å.

(**D**) Gold-standard Fourier shell correlation (FSC) curves for the final reconstructions of the six structural states (top to bottom: monomer, C_2-symmetric dimer, C_2+1 trimer, asymmetric dimer 1, asymmetric dimer 2, and asymmetric dimer 3) based on the FSC = 0.143 criterion.

(**E**) Two orthogonal views (rotated by 180°) of the local resolution maps for the six structural states (arranged in the same order as in **D**). The local resolution color scale (Å) is displayed at the bottom.

(**F**) Angular distribution heatmaps of particles contributing to the final 3D reconstructions for the six corresponding structural states (arranged in the same order as in **D**).

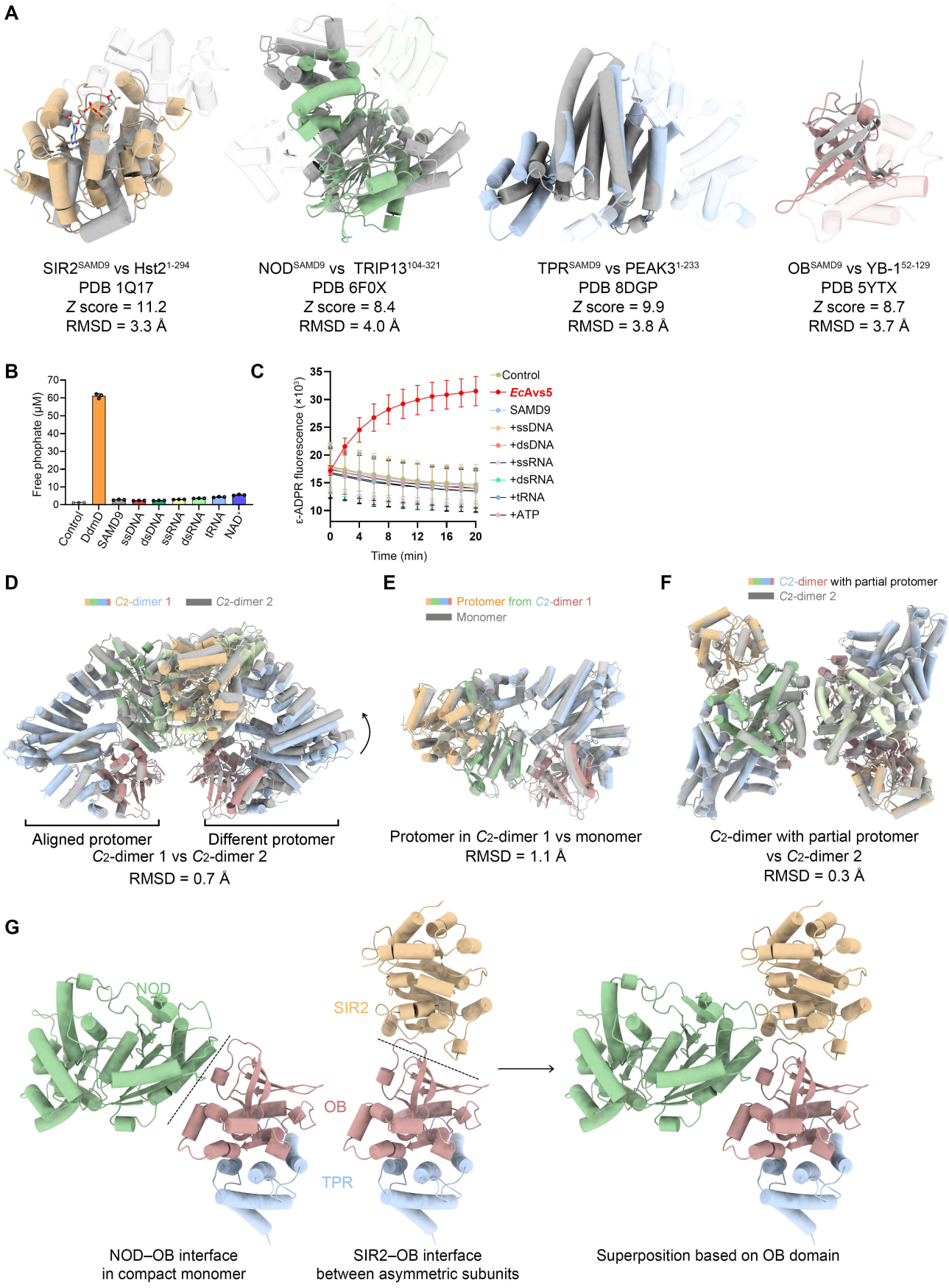
A
SIR2SAMD9 vs Hst21-294
PDB 1Q17
Z score = 11.2
RMSD = 3.3 Å
NODSAMD9 vs TRIP13104-321
PDB 6F0X
Z score = 8.4
RMSD = 4.0 Å
TPRSAMD9 vs PEAK31-233
PDB 8DGP
Z score = 9.9
RMSD = 3.8 Å
OBSAMD9 vs YB-152-129
PDB 5YTX
Z score = 8.7
RMSD = 3.7 Å
B
Free phophate (μM)
Control
DdmD
SAMD9
ssDNA
dsDNA
ssRNA
dsRNA
tRNA
NAD+
C
ε-ADPR fluorescence (×10³)
Time (min)
Control
EcAvs5
SAMD9
+ssDNA
+dsDNA
+ssRNA
+dsRNA
+tRNA
+ATP
D
C2-dimer 1
C2-dimer 2
Aligned protomer
Different protomer
C2-dimer 1 vs C2-dimer 2
RMSD = 0.7 Å
E
Protomer from C2-dimer 1
Monomer
Protomer in C2-dimer 1 vs monomer
RMSD = 1.1 Å
F
C2-dimer with partial protomer
C2-dimer 2
C2-dimer with partial protomer
vs C2-dimer 2
RMSD = 0.3 Å
G
NOD
SIR2
OB
TPR
NOD–OB interface
in compact monomer
SIR2–OB interface
between asymmetric subunits
Superposition based on OB domain

Supplementary Figure S4. Structural and functional characterization of SAMD9C domains, enzymatic activities, and C_2-symmetric dimer conformations

(**A**) Structural superposition of individual SAMD9C domains with their top structural analogs identified by DALI search: SIR2 versus Hst2$^{1–294}$ (PDB 1Q17, *Z* score = 11.2, RMSD = 3.3 Å); NOD versus TRIP13$^{104–321}$ (PDB 6F0X, *Z* score = 8.4, RMSD = 4.0 Å); TPR versus PEAK3$^{1–233}$ (PDB 8DGP, *Z* score = 9.9, RMSD = 3.8 Å); and OB versus YB-1$^{52–129}$ (PDB 5YTX, *Z* score = 8.7, RMSD = 3.7 Å).

(**B**) Structural superposition of SAMD9C C_2-asymmetric dimer 1 (colored by domain as in Figure 1) and dimer 2 (gray), aligned on a single protomer (left, "Aligned protomer"; RMSD = 0.7 Å). The inter-protomer conformational rotation of the adjacent protomer (right, "Different protomer") are indicated by the black curved arrow.

(**C**) *In vitro* ATPase activity of wild-type SAMD9C measured by free phosphate release in the presence or absence of various nucleic acids (ssDNA, dsDNA, ssRNA, dsRNA, tRNA) or NAD^+. DdmD serves as a positive control.

(**D**) Time-course NADase activity of wild-type SAMD9C monitored by ε-ADPR fluorescence in the presence or absence of nucleic acids or ATP. *Ec*Avs5 serves as a positive control for NAD^+ cleavage.

(**E**) Structural alignment of a single protomer from C_2-dimer 1 (colored by domain) against the monomeric state (gray; RMSD = 1.1 Å), highlighting the structural conservation within individual protomers.

(**F**) Superposition of the C_2-dimer containing a partial protomer (colored) onto C_2-dimer 2 (gray; RMSD = 0.3 Å), demonstrating a highly conserved dimer interface and rigid packing.

(**G**) Structural comparison between the intramolecular NOD–OB interface in the compact monomer and the intermolecular SIR2–OB interface between asymmetric subunits. On the left, the two interacting domain pairs are shown separately using the OB–TPR module as a fixed reference, with black dashed lines indicating domain–domain contact interfaces. On the right, structural superposition of the two states based on the OB–TPR module reveals that the intramolecular binding of NOD to OB and the intermolecular binding of SIR2 to OB can occur without an apparent steric clash. Domains are color-coded as in Figure 1.

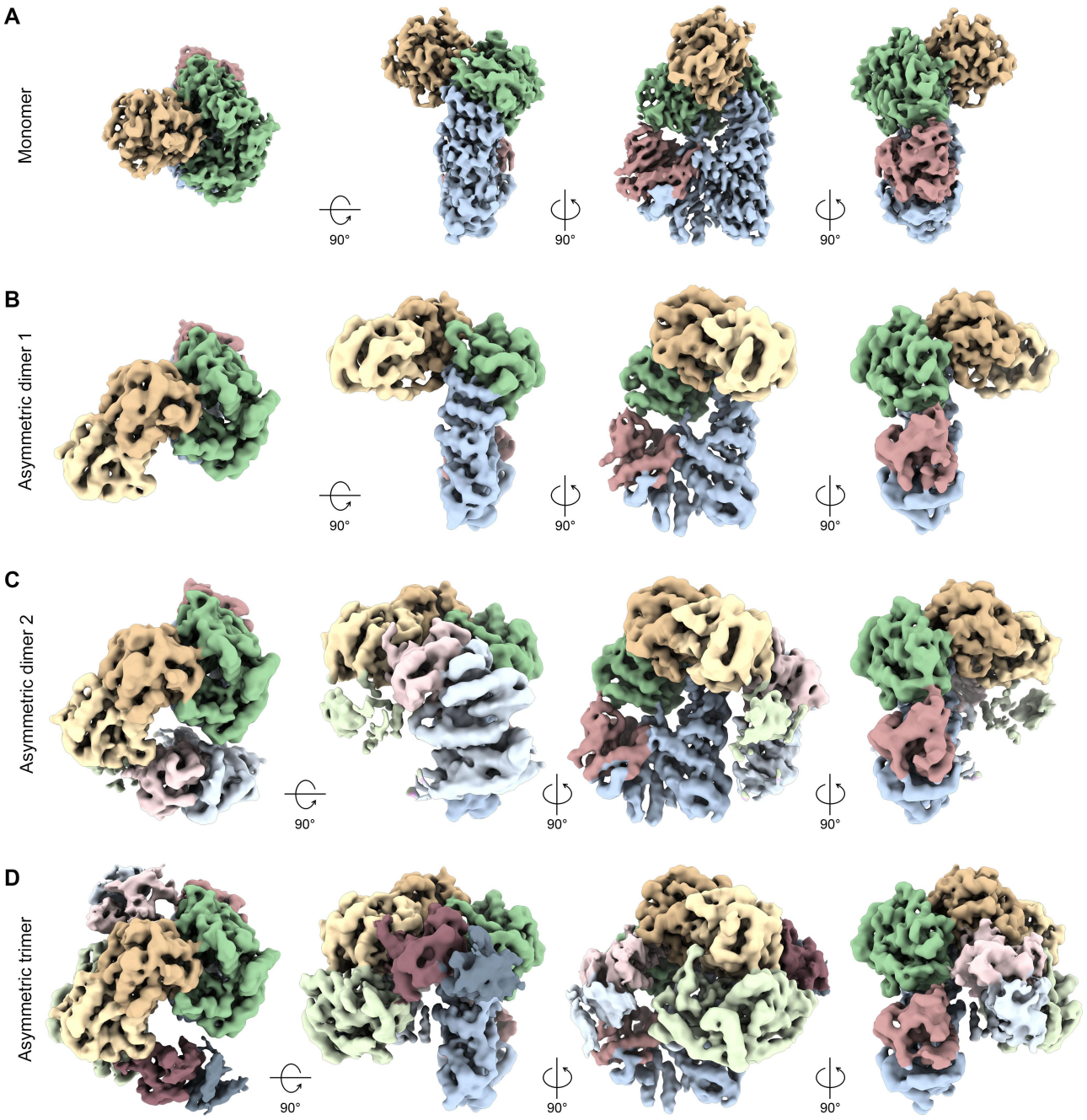

Supplementary Figure S5. Structural comparison of SAMD9C in monomeric and asymmetric oligomeric states

(**A**–**D**) Four orthogonal views of density maps for distinct SAMD9C assembly states captured during single-particle reconstruction, including the monomer (**A**), asymmetric dimer 1 (**B**), asymmetric dimer 2 (**C**), and asymmetric trimer (**D**). Maps are shown in matching orientations across panel rows for direct comparison, highlighting domain rearrangements and protomer heterogeneity across different assembly states. Successive 90° rotations are indicated by orientation arrows. All cryo-EM density maps are segmented and color-coded by domain as defined in Figure 1.

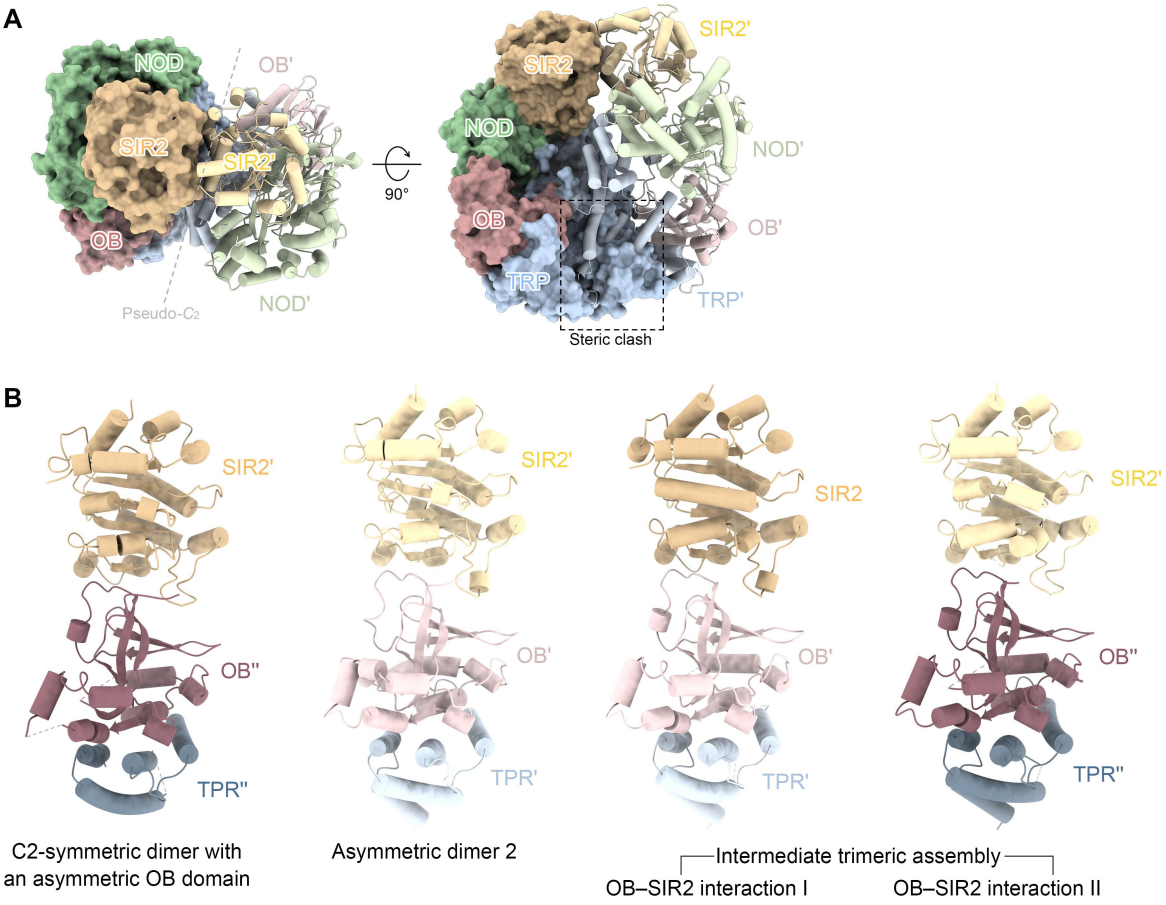

Supplementary Figure S6. Structural analysis of SIR2–SIR2' and SIR2–OB interfaces mediating SAMD9 oligomerization

(**A**) Structural model of a pseudo-C_2-symmetric dimer mediated by SIR2–SIR2' interactions (left). Protomer 1 and protomer 2 are shown in surface and cartoon representations, respectively, with domains colored as in Figure 1. A rotated view reveals apparent steric clashes between the TPR–OB regions of opposing protomers (right, dashed box), suggesting that conformational rearrangement of the NOD–TPR–OB module may be required to accommodate this dimeric assembly.

(**B**) Comparison of SIR2–OB intersubunit interactions across distinct SAMD9C assembly states, including the C_2-dimer engaging an additional OB domain, asymmetric dimer 2, and two distinct SIR2–OB interaction interfaces (I and II) in the intermediate trimer. The SIR2–OB interaction mode is conserved across these oligomeric states. Domains are shown in cartoon representation, with prime notation used to distinguish individual protomers.

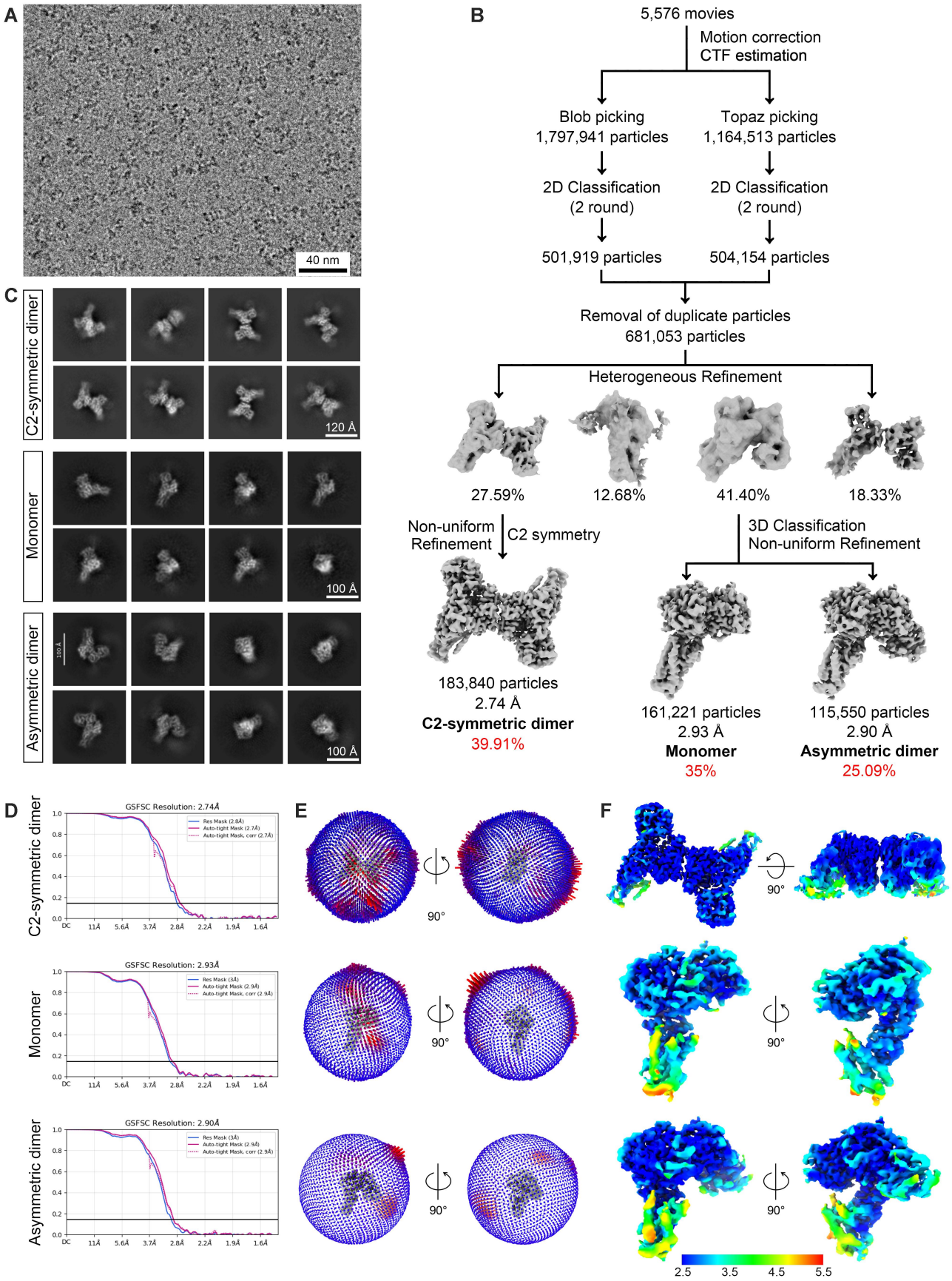
A
40 nm
B
5,576 movies
Motion correction
CTF estimation
Blob picking
1,797,941 particles
Topaz picking
1,164,513 particles
2D Classification
(2 round)
2D Classification
(2 round)
501,919 particles
504,154 particles
Removal of duplicate particles
681,053 particles
Heterogeneous Refinement
27.59%
12.68%
41.40%
18.33%
Non-uniform
Refinement
C2 symmetry
3D Classification
Non-uniform Refinement
183,840 particles
2.74 Å
C2-symmetric dimer
39.91%
161,221 particles
2.93 Å
Monomer
35%
115,550 particles
2.90 Å
Asymmetric dimer
25.09%
C
C2-symmetric dimer
Monomer
Asymmetric dimer
120 Å
100 Å
100 Å
100 Å
D
C2-symmetric dimer
Monomer
Asymmetric dimer
GSFSC Resolution: 2.74Å
GSFSC Resolution: 2.93Å
GSFSC Resolution: 2.90Å
E
90°
90°
90°
F
90°
90°
90°
2.5
3.5
4.5
5.5

Supplementary Figure S7. Cryo-EM data processing and single-particle reconstruction of the AlbA2 and OB domain-truncated SAMD9C variant (SAMD9C$^{\Delta OB}$)

(**A**) Representative cryo-EM micrograph. Scale bar, 40 nm.

(**B**) Flowchart of cryo-EM data processing workflow. From 5,576 movies, initial particle picking yielded 1,797,941 particles via blob picking and 1,164,513 particles via Topaz picking. Following two rounds of 2D classification and duplicate removal, a cleaned dataset of 681,053 particles was subjected to heterogeneous refinement. Subsequent 3D classification, non-uniform refinement, and symmetry application generated three distinct conformational maps: a 2.74 Å map of the C_2-symmetric dimer (183,840 particles) via C_2 symmetry application, as well as a 2.93 Å map of the monomer (161,221 particles) and a 2.90 Å map of the asymmetric dimer (115,550 particles) following further 3D classification and non-uniform refinement.

(**C**) Representative 2D class averages showing distinct structural features for the C_2-symmetric dimer (top), monomer (middle), and asymmetric dimer (bottom) states. Scale bars, 120 Å (for C_2-symmetric dimer) and 100 Å (for monomer and asymmetric dimer).

(**D**) Gold-standard Fourier shell correlation (FSC) curves for the final 3D reconstructions, indicating global resolutions of 2.74 Å (C_2-symmetric dimer), 2.93 Å (monomer), and 2.90 Å (asymmetric dimer) based on the FSC = 0.143 criterion.

(**E**) Angular distribution heatmaps of particles contributing to the final reconstructions of the three structural states (top to bottom: C_2-symmetric dimer, monomer, and asymmetric dimer).

(**F**) Two orthogonal views of the local resolution maps for the C_2-symmetric dimer (top), monomer (middle), and asymmetric dimer (bottom) calculated in cryoSPARC. The local resolution color scale (Å) is displayed at the bottom.

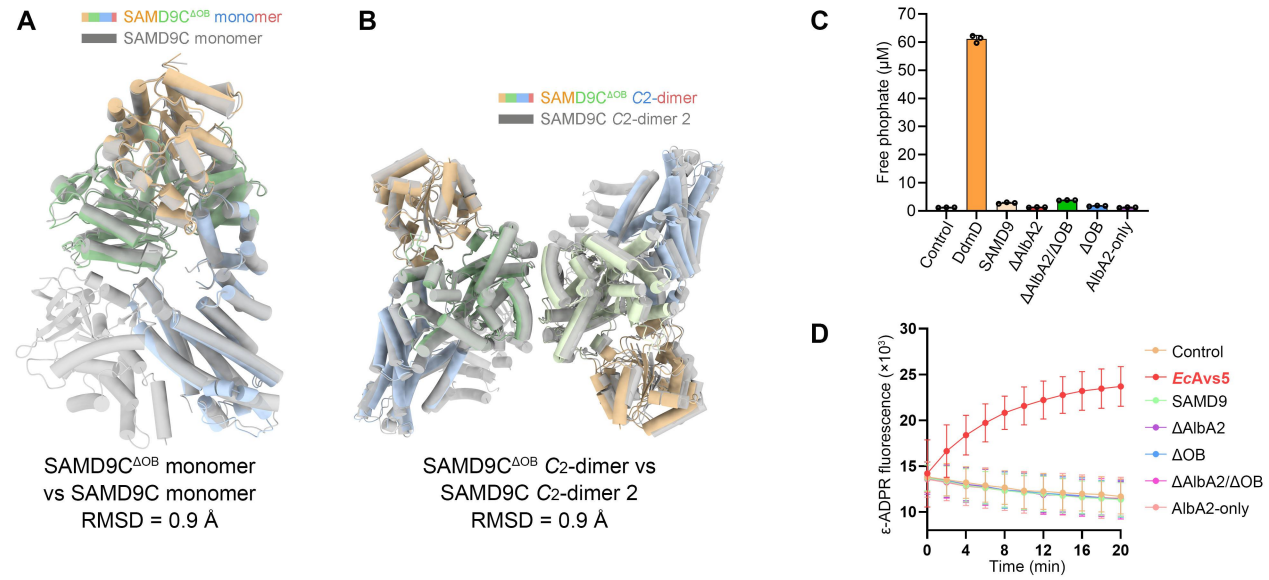
A
SAMD9C^ΔOB monomer
SAMD9C monomer
SAMD9C^ΔOB monomer
vs SAMD9C monomer
RMSD = 0.9 Å
B
SAMD9C^ΔOB C2-dimer
SAMD9C C2-dimer 2
SAMD9C^ΔOB C2-dimer vs
SAMD9C C2-dimer 2
RMSD = 0.9 Å
C
Free phophate (μM)
70
60
50
40
30
20
10
0
Control
DdmD
SAMD9
ΔAlbA2
ΔAlbA2/ΔOB
ΔOB
AlbA2-only
D
ε-ADPR fluorescence (×10³)
30
25
20
15
10
0
4
8
12
16
20
Time (min)
Control
EcAvs5
SAMD9
ΔAlbA2
ΔOB
ΔAlbA2/ΔOB
AlbA2-only

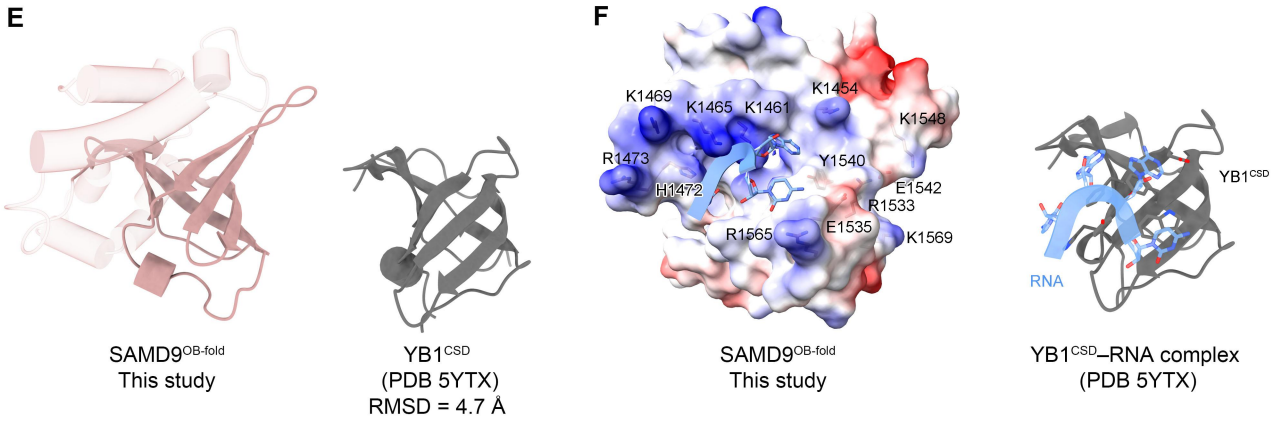
E
SAMD9^OB-fold
This study
YB1^CSD
(PDB 5YTX)
RMSD = 4.7 Å
F
K1469
K1465
K1461
K1454
K1548
R1473
Y1540
H1472
E1542
R1533
R1565
E1535
K1569
SAMD9^OB-fold
This study
YB1^CSD
RNA
YB1^CSD–RNA complex
(PDB 5YTX)

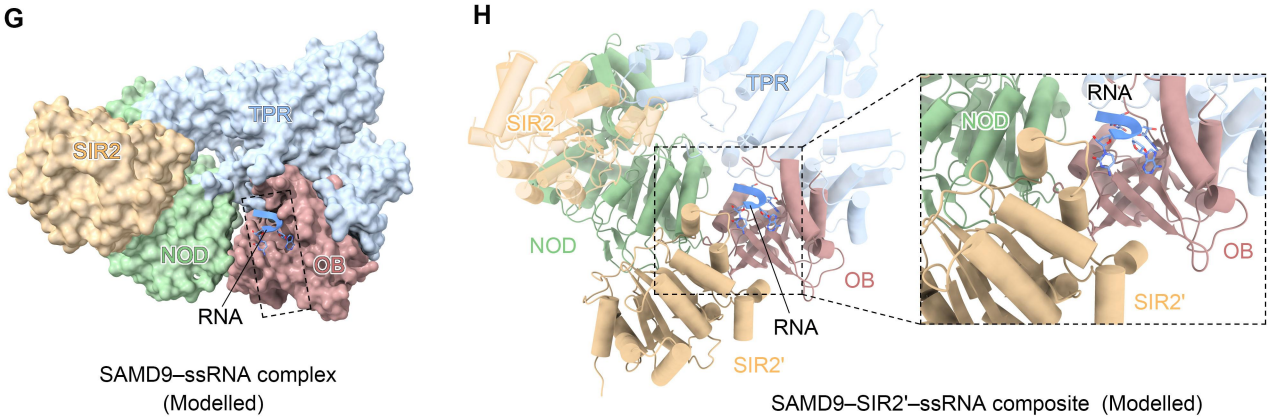
G
TPR
SIR2
NOD
OB
RNA
SAMD9–ssRNA complex
(Modelled)
H
TPR
SIR2
NOD
OB
RNA
SIR2'
RNA
NOD
OB
SIR2'
SAMD9–SIR2'–ssRNA composite (Modelled)

Supplementary Figure S8. Structural and functional characterization of the SAMD9C$^{\Delta OB}$ construct and the putative nucleic acid-binding role of the OB-fold domain

(**A**) Structural superposition of the SAMD9C$^{\Delta OB}$ monomer (colored by domain as in Figure 1) against the wild-type SAMD9C monomer (gray; RMSD = 0.9 Å), demonstrating that truncation of the OB domain does not induce marked structural rearrangements in the remaining core domains.

(**B**) Structural superposition of the SAMD9C$^{\Delta OB}$ C_2-dimer (colored by domain) onto the wild-type SAMD9C C_2-dimer 2 (gray; RMSD = 0.9 Å), showing a conserved dimeric architecture and inter-subunit packing interface.

(**C**) ATPase activity assays of SAMD9C truncation mutants and domain variants (ΔAlbA2, ΔOB, ΔAlbA2/ΔOB, and AlbA2-only), with DdmD as a positive control.

(**D**) Time-course NADase activity assays of SAMD9C truncation mutants and domain variants, with *Ec*Avs5 as a positive control. Data in (**A**–**D**) are presented as mean ± s.d. from three independent experiments (n = 3), represented by individual biological replicate points.

(**E**) Structural comparison of the OB domain of SAMD9 (SAMD9$^{OB\text{-}fold}$, salmon) and its structural analog of human YB-1 (YB1^{CSD}, PDB 5YTX, gray; RMSD = 3.7 Å).

(**F**) Electrostatic surface potential of the AlphaFold-predicted SAMD9$^{OB\text{-}fold}$–ssRNA complex compared with the YB1^{CSD}–RNA complex structure (right, PDB 5YTX). Key residues forming the positively charged RNA-binding groove in SAMD9 are shown as sticks and labeled.

(**G**) Surface representation of the modeled SAMD9C–ssRNA complex. Domains are colored as in Figure 1, with the ssRNA accommodated in the OB domain cleft (dashed box).

(**H**) Composite structural model illustrating the spatial relationship between SAMD9C, ssRNA, and a modeled adjacent SIR2' domain, shown in cartoon representation (left) and close-up view of the RNA-binding interface (right, dashed inset). Modeling indicates that RNA binding to the OB-fold domain does not obviously interfere with either its intramolecular interaction with NOD or its intermolecular interaction with the SIR2' domain.

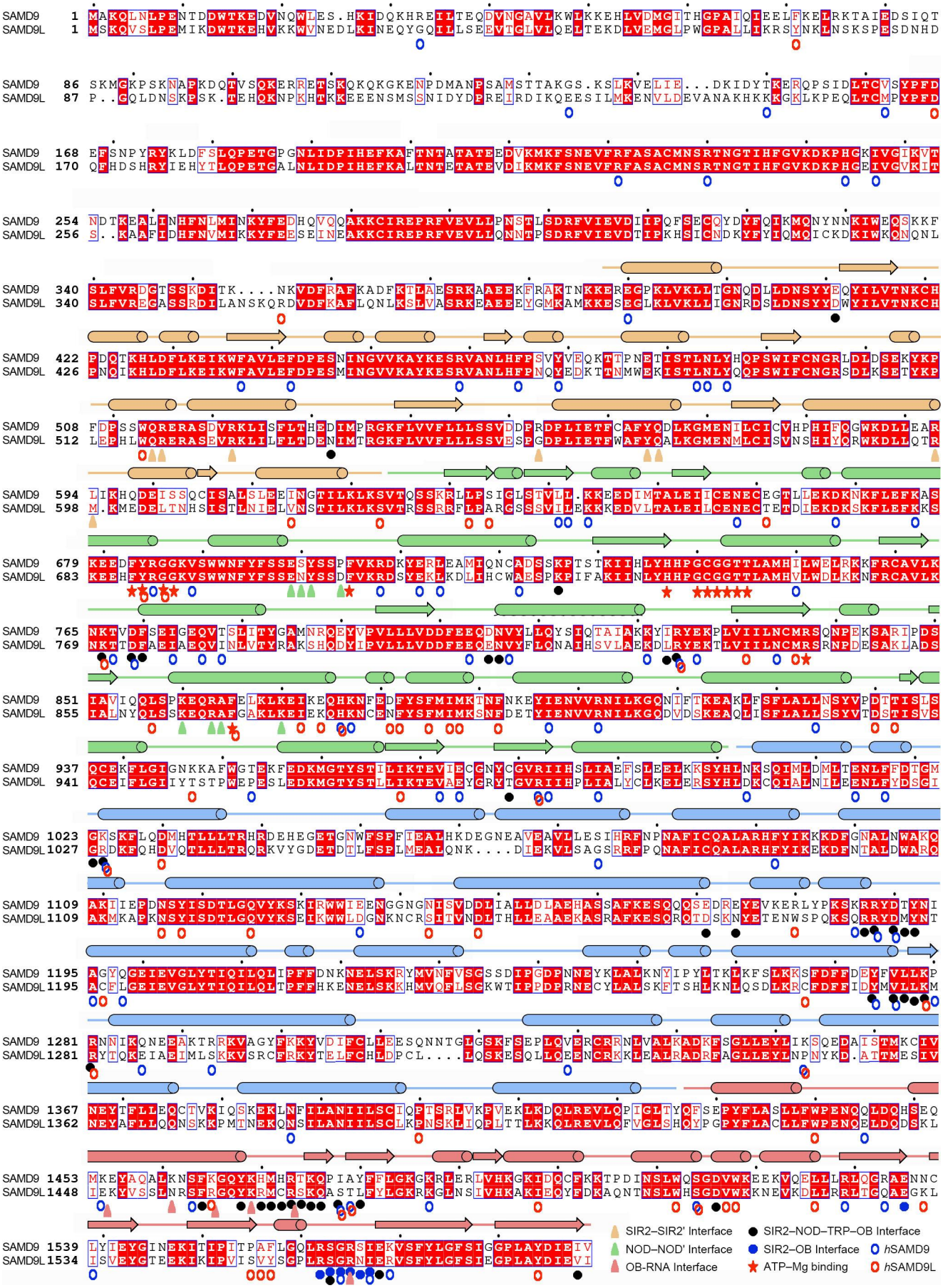
SAMD9
SAMD9L
SIR2–SIR2' Interface
NOD–NOD' Interface
OB-RNA Interface
SIR2–NOD–TRP–OB Interface
SIR2–OB Interface
ATP–Mg binding
hSAMD9
hSAMD9L

Supplementary Figure S9. Sequence alignment of human SAMD9 and SAMD9L

Structure-guided sequence alignment between human SAMD9 (*h*SAMD9, UniProt ID; Q5K651) and SAMD9L (*h*SAMD9L; UniProt ID: Q8IVG5). Secondary structure of solved SAMD9 domains are shown above the alignment and colored according to the domain organization in Figure 1A. Strictly conserved residues are highlighted in red boxes with white letters, and conservative substitutions are indicated in blue frames with red characters. Symbols below the alignment denote residues involved in ATP–Mg^{2+} coordination, nucleic-acid recognition, intraprotomer autoinhibition, and interprotomer assembly. ATP–Mg^{2+}-coordinating residues are marked with red asterisks; intraprotomer autoinhibitory interface residues (SIR2–NOD–TPR–OB interface) with filled black circles; asymmetric interprotomer interface residues (SIR2–OB) with blue circles; symmetric interprotomer interface residues (SIR2–SIR2' and NOD–NOD') with light orange and light green triangles, respectively; and OB–RNA interface residues with salmon triangles. Reported disease-associated variants in *h*SAMD9 and *h*SAMD9L are indicated by blue and red open ellipses, respectively.

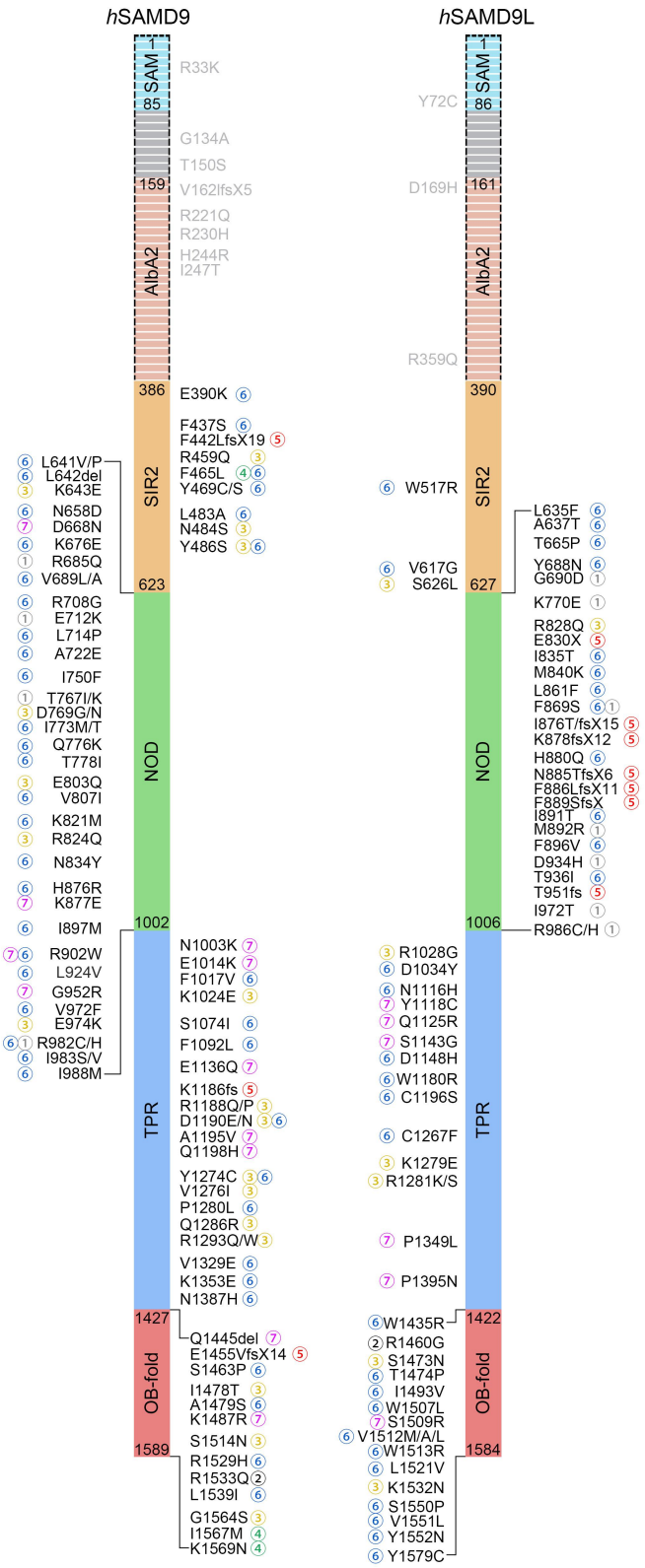

Supplementary Figure S10. Map of disease-associated mutations in human SAMD9 and SAMD9L
Schematic representation of *h*SAMD9 and *h*SAMD9L domain organizations with reported clinical and pathogenic mutations mapped along the primary sequences. Structural domains are color-coded with boundary residue positions corresponding to those in Figure 1A. Circled numbers (1–7) adjacent to individual variants denote the structural and mechanistic categories perturbed by each mutation. Categories (1–4) correspond to the structure-based classifications illustrated by mapping representative variants onto the three-dimensional SAMD9/SAMD9L models in Figure 7A: (1) NOD conformational dynamics and nucleotide-binding sites; (2) OB-domain-mediated nucleic acid sensing; (3) intraprotomer autoinhibitory interfaces; (4) asymmetric SIR2–OB assembly interfaces. Additional categories include (5) buried substitutions predicted to compromise core domain stability; (6) nonsense or frameshift variants leading to truncated products; and (7) variants whose molecular consequences cannot be unambiguously interpreted within the current structural framework. Representative variants mapped onto the 3D structures are presented in Figure 7A.

Table S1. Cryo-EM statistics for monomeric and C_2-symmetric dimeric SAMD9C states

	SAMD9C monomer	**C_2-symmetric dimer 1**	**C_2-symmetric dimer 2**	**C_2 dimer + TPR–OB**
	EMD-82773 PDB: 44OU	EMD-81029 PDB: 27BE	EMD-81030 PDB: 27BF	EMD-81031 PDB: 27BG
Data collection and processing				
Microscope	Titan Krios G4		Titan Krios	
Detector	Falcon 4		K3	
Magnification (nominal/calibrated)	165,000		105,000	
Voltage (kV)	300		300	
Electron exposure ($e^-/Å^2$)	50		50	
Defocus range (μm)	−0.8 to −2.5		−0.8 to −2.5	
Pixel size (Å)	0.731		0.83	
Initial particle images (no.)	3,588,049		2,028,974	
Final particle images (no.)	210,379	123,958	225,953	124,016
Symmetry imposed	C1	C2	C2	C1
Map resolution (Å)	2.80	3.20	3.01	3.38
FSC threshold	0.143	0.143	0.143	0.143
Map resolution range (Å)	2.5–6.0	2.5–6.0	2.5–6.0	2.5–6.0
Model refinement and validation				
Initial model used	AlphaFold-predicted model			
Model resolution (Å)	2.8	3.2	3.0	3.4
FSC threshold	0.5	0.5	0.5	0.5
Model composition				
Chains	1	2	2	3
Non-hydrogen atoms	8,914	16,038	15,736	17,265
Protein residues	1,166	2,280	2,252	2,481
Ligands	1 Mg^{2+}, 1 ATP	2 Mg^{2+}, 2 ATP	2 Mg^{2+}, 2 ATP	2 Mg^{2+}, 2 ATP
***B* factors ($Å^2$)**				
Protein	76.64	128.89	140.31	156.54
Ligand	55.84	78.15	78.23	132.35
R.m.s. deviations				
Bond lengths (Å)	0.002	0.002	0.002	0.002
Bond angles (°)	0.503	0.461	0.382	0.449
Validation				
MolProbity score	1.84	1.43	1.36	1.42
Clash score	9.56	4.40	4.05	4.80
Rotamer outliers (%)	0.11	0.00	0.23	0.07
Ramachandran plot				
Favored (%)	95.24	96.65	97.00	97.03
Allowed (%)	4.67	3.31	2.91	2.81
Disallowed (%)	0.09	0.04	0.09	0.17

Table S2. Cryo-EM statistics for asymmetric SAMD9C oligomeric states

	Asymmetric dimer 1	Asymmetric dimer 2	Asymmetric intermediate trimer
	EMD-81032 PDB: 27BH	EMD-81033 PDB: 27BI	EMD-81034 PDB: 27BJ
Data collection and processing			
Microscope		Titan Krios G4	
Detector		K3	
Magnification (nominal/calibrated)		105,000	
Voltage (kV)		300	
Electron exposure ($e^-/Å^2$)		50	
Defocus range (μm)		−0.8 to −2.5	
Pixel size (Å)		0.83	
Initial particle images (no.)		2,028,974	
Final particle images (no.)	26,959	24,252	35,312
Symmetry imposed	C1	C1	C1
Map resolution (Å)	3.88	3.68	3.86
FSC threshold	0.143	0.143	0.143
Map resolution range (Å)	2.5−6.0	2.5−6.0	2.5−6.0
Model refinement and validation			
Initial model used		AlphaFold-predicted model	
Model resolution (Å)	3.9	3.7	3.9
FSC threshold	0.5	0.5	0.5
Model composition			
Chains	2	2	3
Non-hydrogen atoms	8,510	10,674	13,597
Protein residues	1,372	1,806	2,257
Ligands	1 Mg^{2+}, 1 ATP	1 Mg^{2+}, 1 ATP	2 Mg^{2+}, 2 ATP
***B* factors ($Å^2$)**			
Protein	68.92	77.68	82.19
Ligand	39.42	52.47	68.51
R.m.s. deviations			
Bond lengths (Å)	0.002	0.002	0.002
Bond angles (°)	0.457	0.492	0.488
Validation			
MolProbity score	1.40	1.47	1.93
Clash score	3.43	4.25	4.03
Rotamer outliers (%)	0.00	0.21	0.62
Ramachandran plot			
Favored (%)	96.07	96.15	96.77
Allowed (%)	3.56	3.74	3.10
Disallowed (%)	0.37	0.11	0.14

Table S3. Cryo-EM statistics for the SAMD9C$^{\Delta AlbA2/\Delta OB}$

	Monomer	C_2-symmetric dimer	Asymmetric dimer
	EMD-81045 PDB: 27BZ	EMD-81046 PDB: 27CA	EMD-81047 PDB: 27CB
Data collection and processing			
Microscope		Titan Krios G4	
Detector		Falcon 4	
Magnification (nominal/calibrated)		165,000	
Voltage (kV)		300	
Electron exposure ($e^-/Å^2$)		50	
Defocus range (μm)		−0.8 to −2.5	
Pixel size (Å)		0.731	
Initial particle images (no.)		2,962,454	
Final particle images (no.)	161,221	183,840	115,550
Symmetry imposed	C1	C2	C1
Map resolution (Å)	2.93	2.74	2.90
FSC threshold	0.143	0.143	0.143
Map resolution range (Å)	2.5−6.0	2.5−6.0	2.5−6.0
Model refinement and validation			
Initial model used		AlphaFold-predicted model	
Model resolution (Å)	3.0	2.8	2.9
FSC threshold	0.5	0.5	0.5
Model composition			
Chains	1	2	2
Non-hydrogen atoms	7,039	13,145	8,540
Protein residues	897	1762	1,119
Ligands	1 Mg^{2+}, 1 ATP	2 Mg^{2+}, 2 ATP	1 Mg^{2+}, 1 ATP
***B* factors ($Å^2$)**			
Protein	69.49	102.97	75.81
Ligand	60.04	53.42	40.84
R.m.s. deviations			
Bond lengths (Å)	0.002	0.003	0.002
Bond angles (°)	0.404	0.443	0.479
Validation			
MolProbity score	1.43	1.32	1.47
Clash score	5.44	5.84	6.83
Rotamer outliers (%)	0.14	0.16	0.47
Ramachandran plot			
Favored (%)	97.30	98.50	97.54
Allowed (%)	2.47	1.38	2.37
Disallowed (%)	0.22	0.12	0.09